Growth, processing, and optical properties of epitaxial Er_2O_3 on silicon

C. P. Michael,[1,†] H. B. Yuen,[2] V. A. Sabnis,[2] T. J. Johnson,[1] R. Sewell,[2] R. Smith,[2] A. Jamora,[2] A. Clark,[2] S. Semans,[2] P. B. Atanackovic,[2] and O. Painter[1]

[1]*Department of Applied Physics, California Institute of Technology, Pasadena, CA 91125*
[2]*Translucent, Inc., 952 Commercial St., Palo Alto, CA 94303*
[†] *Corresponding author: cmichael@caltech.edu*

Abstract: Erbium-doped materials have been investigated for generating and amplifying light in low-power chip-scale optical networks on silicon, but several effects limit their performance in dense microphotonic applications. Stoichiometric ionic crystals are a potential alternative that achieve an Er^{3+} density $100\times$ greater. We report the growth, processing, material characterization, and optical properties of single-crystal Er_2O_3 epitaxially grown on silicon. A peak Er^{3+} resonant absorption of 364 dB/cm at 1535 nm with minimal background loss places a high limit on potential gain. Using high-quality microdisk resonators, we conduct thorough C/L-band radiative efficiency and lifetime measurements and observe strong upconverted luminescence near 550 and 670 nm.

OCIS codes: (160.4760) Materials – optical properties; (160.5690) Rare-earch-doped materials; (190.7220) Upconversion; (230.5750) Resonators

References and links

1. L. Pavesi and D. J. Lockwood, eds., *Silicon Photonics* (Springer-Verlag, Berlin, 2004).
2. J. V. Gates, A. J. Bruce, J. Shmulovich, Y. H. Wong, G. Nykolak, M. R. X. Barros, and R. N. Ghosh, "Fabrication of Er doped glass films as used in planar optical waveguides," Mater. Res. Soc. Symp. Proc. **392**, 209–216 (1995).
3. Y. C. Yan, A. J. Faber, H. de Waal, P. G. Kik, and A. Polman, "Erbium-doped phosphate glass waveguide on silicon with 4.1 dB/cm gain at 1.535 μm," Appl. Phys. Lett. **71**, 2922–2924 (1997).
4. P. G. Kik, M. J. A. de Dood, K. Kikoin, and A. Polman, "Excitation and deexcitation of Er^{3+} in crystalline silicon," Appl. Phys. Lett. **70**, 1721–1723 (1997).
5. R. D. Kekatpure, A. R. Guichard, and M. L. Brongersma, "Free-carrier absorption in Si nanocrystals probed by microcavity photoluminescence," in *Conference on Lasers and Electro-Optics (CLEO)*, p. CTuJ3 (Optical Society of America, San Jose, CA, 2008).
6. J. D. Meindl, J. A. Davis, P. Zarkesh-Ha, C. S. Patel, K. P. Martin, and P. A. Kohl, "Interconnect opportunities for gigascale integration," IBM J. Res. & Dev. **46**, 245–263 (2002).
7. M. J. Kobrinsky, B. A. Block, J.-F. Zheng, B. C. Barnett, E. Mohammed, M. Reshotko, F. Roberton, S. List, I. Young, and K. Cadien, "On-chip optical interconnects," Intel Tech. Jour. **8**, 129–141 (2004).
8. R. Soref and J. Larenzo, "All-silicon active and passive guided-wave components for $\lambda = 1.3$ and 1.6 μm," IEEE J. Quantum Electron. **22**, 873–879 (1986).
9. A. Liu, R. Jones, L. Liao, D. Samara-Rubio, D. Rubin, O. Cohen, R. Nicolaescu, and M. Paniccia, "A high-speed silicon optical modulator based on a metal-oxide-semiconductor capacitor," Nature **427**, 615–618 (2004).
10. M. A. Foster, A. C. Turner, J. E. Sharping, B. S. Schmidt, M. Lipson, and A. L. Gaeta, "Broad-band optical parametric gain on a silicon photonic chip," Nature (London) **441**, 960–963 (2006).
11. L. Colace, G. Masini, F. Galluzzi, G. Assanto, G. Capellini, L. D. Gaspare, E. Palange, and F. Evangelisti, "Metal–semiconductor–metal near-infrared light detector based on epitaxial Ge/Si," Appl. Phys. Lett. **72**, 3175–3177 (1998).
12. Y.-H. Kuo, Y. K. Lee, Y. Ge, S. Ren, J. E. Roth, T. I. Kamins, D. A. B. Miller, and J. S. Harris, "Strong quantum-confined Stark effect in germanium quantum-well structures on silicon," Nature (London) **437**, 1334–1336 (2005).

#100542 - $15.00 USD Received 25 Aug 2008; revised 6 Nov 2008; accepted 8 Nov 2008; published 12 Nov 2008

13. A. W. Fang, H. Park, O. Cohen, R. Jones, M. J. Paniccia, and J. E. Bowers, "Electrically pumped hybrid AlGaInAs-silicon evanescent laser," Opt. Express **14**, 9203–9210 (2006).
14. H. Park, A. W. Fang, R. Jones, O. Cohen, O. Raday, M. N. Sysak, M. J. Paniccia, and J. E. Bowers, "A hybrid AlGaInAs-silicon evanescent waveguide photodetector," Opt. Express **15**, 6044–6052 (2007).
15. A. Kasuya and M. Suezawa, "Resonant excitation of visible photoluminescence form an erbium-oxide overlayer on Si," Appl. Phys. Lett. **71**, 2728–2730 (1997).
16. H. Isshiki, M. J. A. de Dood, A. Polman, and T. Kimura, "Self-assembled infrared-luminescent Er–Si–O crystallites on silicon," Appl. Phys. Lett. **85**, 4343–4345 (2004).
17. K. Masaki, H. Isshiki, and T. Kimura, "Erbium-Silicon-Oxide crystalline films prepared by MOMBE," Opt. Mater. **27**, 876–879 (2004).
18. S. Saini, K. Chen, X. Duan, J. Michel, L. C. Kimerling, and M. Lipson, "Er_2O_3 for high-gain waveguide amplifiers," J. Electron. Mater. **33**, 809–814 (2004).
19. A. M. Grishin, E. V. Vanin, O. V. Tarasenko, S. I. Khartsev, and P. Johansson, "Strong broad *C*-band room-temperature photoluminescence in amorphous Er_2O_3 film," Appl. Phys. Lett. **89**, 021114 (2006).
20. K. Suh, J. H. Shin, S.-J. Seo, and B.-S. Bae, "Large-scale fabrication of single-phase Er_2SiO_5 nanocrystal aggregates using Si nanowires," Appl. Phys. Lett. **89**, 223102 (2006).
21. E. Desurvire, *Erbium-doped Fiber Amplifiers: Principles and Applications* (John Wiley & Sons, Inc., New York, 2002).
22. P. B. Atanackovic, "Rare earth-oxides, rare earth-nitrides, rare earth-phosphides, and ternary alloys with silicon," U.S. Patent 7199015 (Dec. 28, 2004).
23. R. Xu, Y. Y. Zhu, S. Chen, F. Xue, Y. L. Fan, X. J. Yang, and Z. M. Jiang, "Epitaxial growth of Er_2O_3 films on Si(001)," J. Cryst. Growth **277**, 496–501 (2005).
24. J. B. Gruber, J. R. Henderson, M. Muramoto, K. Rajnak, and J. G. Conway, "Energy levels of single-crystal erbium oxide," J. Chem. Phys. **45**, 477–482 (1966).
25. N. C. Chang, J. B. Gruber, R. P. Leavitt, and C. A. Morrison, "Optical spectra, energy levels, and crystal-field analysis of tripositive rare earth ions in Y_2O_3. I. Kramers ions in C_2 sites," J. Chem. Phys. **76**, 3877–3889 (1982).
26. R. P. Leavitt, J. B. Gruber, N. C. Chang, and C. A. Morrison, "Optical spectra, energy levels, and crystal-field analysis of tripositive rare-earth ions in Y_2O_3. II. Non-Kramers ions in C_2 sites," J. Chem. Phys. **76**, 4775–4788 (1982).
27. H. J. Osten, E. Bugiel, M. Czernohorsky, Z. Elassar, O. Kirfel, and A. Fissel, "Molecular Beam Epitaxy of Rare-Earth Oxides," in *Rare Earth Oxide Thin Films*, M. Fanciulli and G. Scarel, eds. (Springer-Verlag, Berlin, 2007).
28. The Er_2O_3(111) orientation is rotated 180° about the Si(111) surface normal.
29. The short wavelengths (S), conventional (C), and long wavelengths (L) telecommunications windows (bands) are relative to the region of lowest optical loss in silica fiber ($\lambda \approx 1550$ nm) and occur at 1460–1530 nm, 1530–1565 nm, and 1565–1625 nm, respectively. These designations are not strictly applied in this report as that the absorption extends into the E-band (extended, 1360–1460 nm) and the emission in Fig. 8 continues through the U-band (ultralong wavelengths, 1625–1675 nm).
30. H. Isshiki, T. Ushiyama, and T. Kimura, "Demonstration of ErSiO superlattice crystal waveguide toward optical amplifiers and emitters," Phys. Stat. Sol. A **205**, 52–55 (2008).
31. H. Ono and T. Katsumata, "Interfacial reactions between thin rare-earth-metal oxide films and Si substrates," Appl. Phys. Lett. **78**(13), 1832–1834 (2001).
32. B. J. Ainslie, "A Review of the fabrication and properties of Erbium-doped fibers for optical amplifiers," IEEE J. Lightwave Technol. **9**, 220–227 (1991).
33. M. Borselli, T. J. Johnson, and O. Painter, "Beyond the Rayleigh scattering limit in high-Q silicon microdisks: theory and experiment," Opt. Express **13**, 1515 (2005).
34. C. P. Michael, M. Borselli, T. J. Johnson, C. Chrystal, and O. Painter, "An optical fiber-taper probe for wafer-scale microphotonic device characterization," Opt. Express **15**(8), 4745–4752 (2007).
35. K. Srinivasan, A. Stintz, S. Krishna, and O. Painter, "Photoluminescence measurements of quantum-dot-containing semiconductor microdisk resonators using optical fiber taper waveguides," Phys. Rev. B **72**, 205318 (2005).
36. J. B. Gruber, K. L. Nash, D. K. Sardar, U. V. Valiev, N. Ter-Gabrielyan, and L. D. Merkle, "Modeling optical transitions of $Er^{3+}(4f^{11})$ in C_2 and C_{3i} sites in polycrystalline Y_2O_3," J. Appl. Phys. **104**(2), 023101 (2008).
37. J. B. Gruber, R. P. Leavitt, C. A. Morrison, and N. C. Chang, "Optical spectra, energy levels, and crystal-field analysis of tripositive rare-earth ions in Y_2O_3. IV. C_{3i} sites," J. Chem. Phys. **82**, 5373–5378 (1985).
38. The intrinsic loss rate (γ_i) and loss coefficient (α_i) are related through the material- and device-dependent group velocity (v_g): $\alpha_i = \gamma_i / v_g$.
39. M. J. Weber, "Radiative and multiphonon relaxation of rare-earth ions in Y_2O_3," Phys. Rev. **171**, 283–291 (1968).
40. L. A. Riseberg and M. J. Weber, "Relaxation phenomena in rare-earth luminescence," in *Progress in Optics*, vol. XIV, E. Wolf, ed. (North-Holland, Amsterdam, 1976).
41. L. A. Riseberg and H. W. Moos, "Multiphonon orbit-lattice relaxation of excited states of rare-earth ions in crystals," Phys. Rev. **174**, 429–438 (1968).

#100542 - $15.00 USD Received 25 Aug 2008; revised 6 Nov 2008; accepted 8 Nov 2008; published 12 Nov 2008

42. G. Schaack and J. A. Koningstein, "Phonon and electronic Raman spectra of cubic rare-earth oxides and isomorphous yttrium oxide," J. Opt. Soc. Am. **60**, 1110–1115 (1970).
43. L. G. V. Uitert and L. F. Johnson, "Energy transfer between rare-earth ions," J. Chem. Phys. **44**, 3514–3522 (1966).
44. D. L. Dexter and J. H. Schulman, "Theory of concentration quenching in inorganic phosphors," J. Chem. Phys. **22**, 1063–1070 (1954).
45. W. B. Gandrud and H. W. Moos, "Rare-earth infrared lifetimes and exciton migration rates in trichloride crystals," J. Chem. Phys. **49**, 2170–2182 (1968).
46. M. J. Weber, "Luminescence decay by energy migration and transfer: Observation of diffusion-limited relaxation," Phys. Rev. B **4**, 2932–2939 (1971).
47. J. P. van der Ziel, L. Kopf, and L. G. Van Uitert, "Quenching of Tb^{3+} luminescence by direct transfer and migration in aluminum garnets," Phys. Rev. B **6**, 615–623 (1972).
48. R. J. Birgeneau, "Mechanisms of energy transport between rare-earth ions," Appl. Phys. Lett. **13**, 193–195 (1968).
49. E. Okamoto, M. Sekita, and H. Masui, "Energy transfer between Er^{3+} ions in LaF_3," Phys. Rev. B **11**, 5103–5111 (1975).
50. N. Nikonorov, A. Przhevuskii, M. Prassas, and D. Jacob, "Experimental determination of the upconversion rate in erbium-doped silicate glasses," Appl. Opt. **38**, 6284–6291 (1999).
51. P. G. Kik and A. Polman, "Cooperative upconversion as the gain-limiting factor in Er doped miniature Al_2O_3 optical waveguide amplifiers," J. Appl. Phys. **93**, 5008–5012 (2003).
52. S. A. Pollack, D. B. Chang, and N. L. Moise, "Upconversion-pumped infrared erbium laser," J. Appl. Phys. **60**, 4077–4086 (1986).
53. P. Xie and S. C. Rand, "Continuous-wave, pair-pumped laser," Opt. Lett. **15**, 848–850 (1990).
54. P. Xie and S. C. Rand, "Visible cooperative upconversion laser in $Er:LiYF_4$," Opt. Lett. **17**, 1198–1200 (1992).
55. M. Borselli, T. J. Johnson, and O. Painter, "Accurate measurement of scattering and absorption loss in microphotonic devices," Opt. Lett. **32**, 2954–2956 (2007).
56. K. Srinivasan, O. Painter, A. Stintz, and S. Krishna, "Single quantum dot spectroscopy using a fiber taper waveguide near-field optic," Appl. Phys. Lett. **91**, 091102 (2007).
57. K. Srinivasan and O. Painter, "Optical fiber taper coupling and high-resolution wavelength tuning of microdisk resonators at cryogenic temperatures," Appl. Phys. Lett. **90**, 031114 (2007).
58. C. Zinoni, B. Alloing, C. Monat, V. Zwiller, L. H. Li, A. Fiore, L. Lunghi, A. Gerardino, H. de Riedmatten, H. Zbinden, and N. Gisin, "Time-resolved and antibunching experiments on single quantum dots at 1300 nm," Appl. Phys. Lett. **88**, 131102 (2006).
59. B. E. Little and S. T. Chu, "Estimating surface-roughness loss and output coupling in microdisk resonators," Opt. Lett. **21**, 1390–1392 (1996).
60. J. E. Heebner, T. C. Bond, and J. S. Kallman, "Generalized formulation for performance degradations due to bending and edge scattering loss in microdisk resonators," Opt. Express **15**, 4452–4473 (2007).
61. H. A. Haus, *Waves and Fields in Optoelectronics* (Prentice-Hall, Inc., Englewood Cliffs, New Jersey, 1984).
62. D. S. Weiss, V. Sandoghdar, J. Hare, V. Lefevre-Seguin, J.-M. Raimond, and S. Haroche, "Splitting of high- Q Mie modes induced by light backscattering in silica microspheres," Opt. Lett. **20**, 1835–1837 (1995).
63. M. L. Gorodetsky, A. D. Pryamikov, and V. S. Ilchenko, "Rayleigh scattering in high-Q microspheres," J. Opt. Soc. Am. B **17**, 1051–1057 (2000).
64. K. Srinivasan and O. Painter, "Mode coupling and cavity-quantum-dot interactions in a fiber-coupled microdisk cavity," Phys. Rev. A **75**, 023814 (2007).
65. S. M. Spillane, T. J. Kippenberg, O. J. Painter, and K. J. Vahala, "Ideality in a fiber-taper-coupled microresonator system for application to cavity quantum electrodynamics," Phys. Rev. Lett. **91**, 043902 (2003).
66. C. P. Michael, K. Srinivasan, T. J. Johnson, O. Painter, K. H. Lee, K. Hennessy, H. Kim, and E. Hu, "Wavelength- and material-dependent absorption in GaAs and AlGaAs microcavities," Appl. Phys. Lett. **90**, 051108 (2007).
67. M. Borselli, K. Srinivasan, P. E. Barclay, and O. Painter, "Rayleigh scattering, mode coupling, and optical loss in silicon microdisks," Appl. Phys. Lett. **85**, 3693 (2004).
68. S. Strauf, K. Hennessy, M. T. Rakher, Y.-S. Choi, A. Badolato, L. C. Andreani, E. L. Hu, P. M. Petroff, and D. Bouwmeester, "Self-tuned quantum dot gain in photonic crystal lasers," Phys. Rev. Lett. **96**, 127404 (2006).
69. The higher order quasi-TE modes have large bending losses ($Q < 100$) and are poorly phase-matched to the taper waveguide. Since they cannot be observed in transmission or taper-collected PL, all necessary parameters are obtained through finite element simulations.
70. P. C. Becker, N. A. Olsson, and J. R. Simpson, *Erbium-Doped Fiber Amplifiers: Fundementals and Technology*, Optics and Photonics (Academic Press, San Diego, 1999).

Significant progress in the last decade has been made developing passive and active silicon optical components; however, efficient generation of light within a Si platform remains a technical and commercial challenge [1]. Efforts to incorporate Er^{3+} into the Si material system, with erbium's emission in the 1550-nm telecommunications band, have met with limited success.

#100542 - $15.00 USD Received 25 Aug 2008; revised 6 Nov 2008; accepted 8 Nov 2008; published 12 Nov 2008

Amorphous Er^{3+}-doped glass waveguides on Si provide insufficient gain (<4 dB/cm [2, 3]) for dense photonic integration, while doped silicon allotropes are limited by other effects such as Auger recombination [4] and free-carrier absorption [5]. Here we describe the characterization of stoichiometric single-crystal Er_2O_3-on-Si (EOS) grown by atomic layer epitaxy. We measure a peak resonant absorption of 364 dB/cm at 1535 nm and negligible background absorption (<3 dB/cm). The observed radiative efficiency from 1520–1650 nm is 0.09% with cooperative upconversion producing strong green and red emission for Er^{3+} excitation levels as low as 2%. Further development of EOS as multi-component rare-earth oxides, and their superlattices with Si, may allow for tailored emission spectra, controlled upconversion, and electrically injected light emission.

Spurred by the growing power consumption of high-speed electrical interconnects for multi-core processors [6], optical networks have become an attractive option to achieve Tb/s on-chip bandwidth [7]. Following the initial demonstration of silicon waveguide devices [8], there has been significant development in adding optical functionality to silicon microelectronics and, similarly, applying the efficiency and infrastructure of modern CMOS processing to optical telecommunication components. While silicon exhibits low loss across the 1300-nm and 1550-nm telecommunication windows, unstrained silicon lacks any significant Pockels coefficient and produces little emission from its 1.1 eV indirect bandgap [1]. Free-carrier dispersion and four-wave mixing provide some inherent active functionality such as modulation with rates exceeding 1 GHz [9] and wavelength conversion [10], but considerable research, especially concerning light emission and detection, has focused on integrating silicon with other optical materials such as SiGe [11, 12] and the III-Vs [13, 14]. In this work we describe the growth, processing, and optical properties of single-crystal Er_2O_3-on-Si (EOS). Similar to stoichiometric polycrystalline Er^{3+} materials [15–20], EOS allows for a 100-fold increase in Er^{3+} concentration over conventional Er-doped glasses [21], making it an attractive material for on-chip emission and amplification in the 1550-nm wavelength band. Developed simultaneously for optoelectronic [22] and high-κ dielectric [23] applications, epitaxially grown Er_2O_3 films can be incorporated into precisely controlled heterostructures and superlattices, which may also allow for efficient electrical injection. Oxides incorporating multiple cation species provide additional flexibility in designing the emission spectrum and dynamics as a number of rare-earth ions (Er^{3+}, Yb^{3+}, Nd^{3+}, Dy^{3+}, etc.) are interchangeable in the $(RE)_2O_3$ lattice [24–26]. Beyond application to chip-based optical networks, the strong cooperative upconversion within these films may also be used for visible light generation in solid-state lighting and displays and infrared-to-visible energy conversion in photovolatics.

1. Growth

As shown in Fig. 1(a), single-crystal stoichiometric Er_2O_3 can be grown via atomic layer epitaxy on Si(111) or Si(100) on-axis wafers without a buffer layer. Like most trivalent lanthanide oxides [27], the film has a bixbyite crystal structure oriented along $Er_2O_3(111)$ [$Er_2O_3(110)$] on Si(111) [Si(100)] [28]. To minimize both erbium silicide formation and native SiO_x growth, the O_2:Er ratio during deposition is 1:5. High growth temperatures between 650–900 °C result in more homogeneous films [measured by transmission electron microscopy (TEM) and x-ray diffraction (XRD)], smoother surfaces [$\sim$1 nm roughness by atomic force microscopy (AFM), TEM, and reflection high-energy electron diffraction (RHEED)], and stronger C-band [29] photoluminescence with a narrower linewidth at 1536 nm [Fig. 2(a)]. Films on Si(111) are consistently higher quality and have been grown up to 200 nm thick. We observe no evidence of erbium clustering using TEM or visible upconversion [30]. In post-growth XRD analysis, the dominant peaks in Fig. 1(b) are due to the substrate's Si$\{111\}$ and film's $Er_2O_3\{111\}$ planes. Lesser peaks are associated with additional lines from the X-ray source (K_β, W) and with dif-

#100542 - $15.00 USD Received 25 Aug 2008; revised 6 Nov 2008; accepted 8 Nov 2008; published 12 Nov 2008

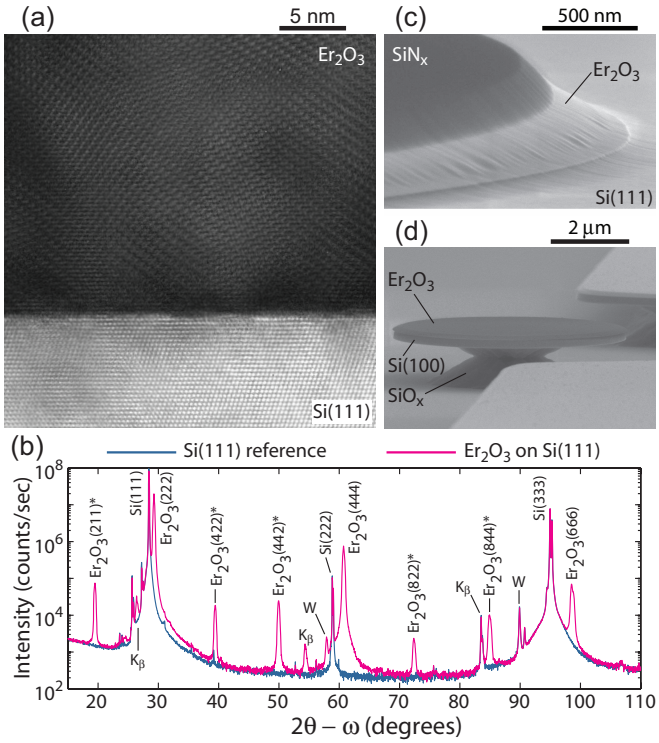

Fig. 1. Er_2O_3 Growth and Processing. (a) TEM image of Er_2O_3-Si interface. (b) XRD spectrum for Er_2O_3 on Si(111) and a reference Si(111) sample; the ($\star$) peaks designate strained layers (see §A.1). (c) SEM image of Er_2O_3 microdisk edge prior to the SF_6 undercut. (d) Hybrid Er_2O_3-Si microdisk (78 nm Er_2O_3, 188 nm Si, 1 μm SiO_x) after the final HF undercut of the buried oxide.

fraction from minority Er_2O_3 phases; there is no XRD evidence of erbium silicates or silicides at the Er_2O_3-Si interface [23,31]. The {211}, {442}, and {822} families of peaks correspond to slightly strained volumes with surfaces nearly parallel to the dominant (111) surface. Given the EOS films' homogeneous TEM cross sections and the relative intensities of the secondary XRD peaks, the minority phases compose a small fraction of the material. In addition to growth of Er_2O_3 on Si substrates, we have also demonstrated growth on the top Si device layer of (100)-oriented silicon-on-insulator substrates, as shown in Fig. 1(d).

2. Processing

Chip-based photonics require a number of micron- and sub-micron-scale elements, such as waveguides and resonators. These resonators can be used to form on-chip lasers and filters or, as in this work, to sensitively and accurately determine the optical properties of a given material. Here we are interested in low-loss microdisk cavities in which the light "whispers" around the disk's periphery—i.e. whispering gallery modes (WGMs). To minimize scattering in these devices, processing techniques must be developed that produce little surface roughness. At room temperature, we have found Er_2O_3 is nearly impervious to HF (49% by wt.), KOH (30% by wt.), Piranha, HCl (37% by wt.), and reactive ion etching (RIE) using C_4F_8:SF_6. At 70°C, concentrated HCl, H_2SO_4, and KOH etch Er_2O_3, but they leave ragged edges and appear

#100542 - $15.00 USD Received 25 Aug 2008; revised 6 Nov 2008; accepted 8 Nov 2008; published 12 Nov 2008

to be slightly anisotropic. Reactive ion dry etching with a Cl_2-catalyzed plasma will etch the material but not remove it from the surface—droplets of involatile etch byproducts form on the wafer. Because these deposits do not sublimate at process temperatures ($\leq$205 °C) but are water soluble, we believe these droplets are erbium chlorides, which are known to have a low vapor pressure [32]. Rather than chemically etching the Er_2O_3 device layer, we use ion milling with high Ar^+ flux and high DC bias.

To fabricate Er_2O_3 microdisk resonators, a 400-nm low-stress SiN_x hard mask is grown on the Er_2O_3-Si wafer by plasma enhanced chemical vapor deposition. The microdisk patterns are defined using electron-beam lithography and resist reflow [33] and then are transferred to the SiN_x using a C_4F_8:SF_6 RIE. We then mill the Er_2O_3 with an Ar^+ plasma. The Ar^+ mill exhibits approximately 1:1 selectivity with the SiN_x hard mask; the resulting side walls [Fig. 1(c)] feature mild striations due to magnification of residual roughness in the EOS. Finally, an isotropic SF_6 dry etch simultaneously partially undercuts the silicon substrate and removes the remaining SiN_x mask. Processing hybrid Er_2O_3-Si resonators from Er_2O_3-SOI wafers, as in Fig. 1(d), employs the same SiN_x hard mask and Ar^+ mill. With the Er_2O_3 layer acting as a mask, we etch the silicon device layer with an anisotropic C_4F_8:SF_6 RIE and undercut the buried oxide with concentrated HF. Many samples are prepared to optimize the process parameters at each step in order to minimize the microdisk side wall roughness. The measurements described here concern $\sim$150-nm thick Er_2O_3 on Si(111) and Er_2O_3 microdisks with a radius of $\sim 20\,\mu$m.

3. Optical properties

Once the SiN_x is removed and the disks are undercut, the emission and absorption properties of Er_2O_3 are investigated using dimpled fiber taper waveguides [34]. Mounted to a three-axis 50-nm encoded stage, placing the taper in the near field of the disk produces controllable and stable cavity-waveguide coupling. A bank of tunable diode lasers (spanning 963–993 nm and 1420–1625 nm, linewidth $<$300 kHz) were used to characterize the disks' WGMs and excite the Er^{3+} optical transitions. The fiber taper also offers high photoluminescence collection efficiency [35]. Once fiber coupled, the pump and emission can be easily demuxed for sensitive pump-probe and pulsed measurements. Extensive details are available in §A.2–A.3.

3.1. $^4I_{13/2}\rightarrow{}^4I_{15/2}$ absorption and emission spectra

Since the crystal fields are needed to mix states of opposite parity for electric-dipole transitions, ions on the low-symmetry lattice sites (C_2, 24 of 32 sites/unit cell) are optically active while the remaining high-symmetry sites (C_{3i}) experience weaker magnetic-dipole transitions [24]. To observe the Stark-split structure for the $^4I_{13/2}\rightarrow{}^4I_{15/2}$ transitions in this crystalline host, we measure both the room temperature photoluminescence (PL) and absorption spectra. We obtain the emission spectrum by placing the fiber taper in contact with an undercut part of the film and pumping at $\lambda = 981.4$ nm. The fiber-collected luminescence [Fig. 2(a)] displays little inhomogeneous broadening of the Er^{3+} transitions compared to amorphous hosts, and is qualitatively similar to the spectrum reported for polycrystalline Er_2O_3 deposited by pulsed-laser ablation [19]. In comparison to large crystals of Er_2O_3 and dilute Er-doped Y_2O_3 produced by flame fusion [24, 36], the low temperature PL spectrum of EOS exhibits more broadening, also shown in Fig. 2(a).

The absorption spectrum can be determined by fitting the low-power intrinsic loss rate of many fundamental WGMs (one radial antinode of the electric field). While this WGM-linewidth method gives a digital rather than continuous spectrum, it involves measuring spectral widths rather than intensity changes (see §A.3), and coupling losses are insignificant and easily calculated from cavity-waveguide loading. The resulting spectrum [Fig. 2(b)] again reflects the weak inhomogeneous broadening of the Er^{3+} transitions and qualitatively agrees with the

#100542 - $15.00 USD Received 25 Aug 2008; revised 6 Nov 2008; accepted 8 Nov 2008; published 12 Nov 2008

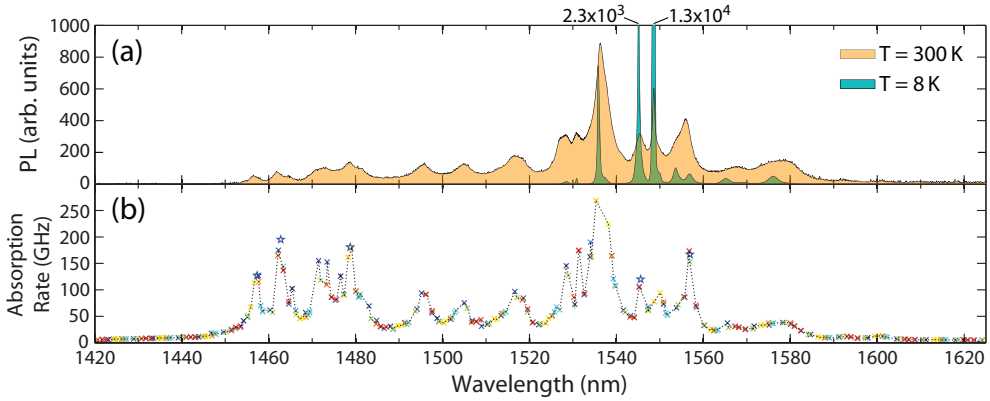

Fig. 2. Emission and absorption spectra. (a) Thin-film PL spectrum at 300 K and 8 K while pumping at 981 nm. The dominant peaks at 8 K are presented off the scale to make smaller features more visible. Emission is observed for ions on both C_2 and C_{3i} sites; the peaks at 1535.8 nm and 1548.6 nm correspond to the transition between the lowest Stark levels of the ${}^4I_{13/2}$ and ${}^4I_{15/2}$ manifolds on the C_2 and C_{3i} sites, respectively [24, 36, 37]. (b) Composite absorption spectrum. Different color $\times$'s correspond to the intrinsic linewidths for modes of different microdisks; the $\star$'s correspond to absorption peaks inferred from non-Lorentzian cavity resonances (see §A.3).

peaks' positions and widths in the PL spectrum. Accounting for material and modal dispersion with scattering losses bound at $<1\%$ of the peak values, the absorption maxima of 267.0 GHz at 1535 nm and 175.4 GHz at 1479 nm correspond to 83.9 cm^{-1} and 56.2 cm^{-1}, respectively [38]. The narrow peaks and low losses in the tails further indicate there is little background absorption, and all 83.9 cm^{-1} (364 dB/cm) can be attributed to resonant ${}^4I_{15/2} \rightarrow {}^4I_{13/2}$ excitation, which sets a high maximum value for potential gain.

3.2. *Upconversion behavior*

While the 1450–1650 nm band is most useful for hybrid Er^{3+}-silicon optical networks, upconversion into visible transitions is also present and has been partly investigated for polycrystalline EOS [15, 18]. We determine the upconversion spectrum by transferring a small piece ($\sim 2\,\mu m^2 \times 150$ nm) of Er_2O_3 onto the fiber taper and pumping with <3 mW at 1536.7 nm. The taper-collected PL is then measured in a spectrometer with a silicon CCD camera. The visible PL contains emission from many levels with significant emission near 550 nm and 670 nm and exhibits little inhomogeneous broadening, as in Fig. 2(a). The pump-power dependence [Fig. 3(c)] of the three primary upconversion bands provides insight into the specific upconversion mechanism [Fig. 3(d)]. The nearly quadratic dependence of the 800 nm emission suggests pair-wise upconversion out of the ${}^4I_{13/2}$ multiplet followed by excited-state absorption or a second upconversion event (${}^4I_{9/2} + {}^4I_{13/2} \rightarrow {}^2H_{11/2}$) to produce the nearly cubic dependence at 550 nm and 670 nm. Subsequent absorption or energy transfer then connects ${}^2H_{11/2}/{}^4S_{3/2}$ to even higher levels with energies in the near UV.

3.3. *Effective ${}^4I_{13/2}$ lifetime*

Depopulation of ${}^4I_{13/2}$ by cooperative upconversion adds an additional complication to measuring the ${}^4I_{13/2} \rightarrow {}^4I_{15/2}$ lifetime. To mitigate the upconversion effects, fluorescence de-

#100542 - $15.00 USD Received 25 Aug 2008; revised 6 Nov 2008; accepted 8 Nov 2008; published 12 Nov 2008

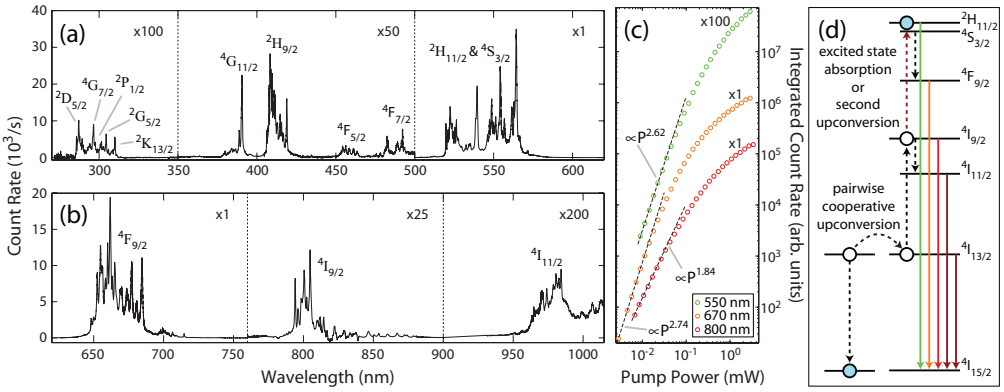

Fig. 3. Upconversion behavior. (a,b) Fiber-taper collected Er_2O_3 upconversion spectrum while pumping at 1536.7 nm; spectroscopic identifications are made by comparison to known Er^{3+} transitions back to $^4I_{15/2}$ [24]. NB: the scale is varied across the spectrum to make weaker transitions more visible. The relative intensities in (a,b) may not reflect the actual strength of each transition because we are unable to correct for the unknown taper collection efficiency across the visible range. (c) Pump-power dependence for the integrated PL in the 550 nm, 670 nm, and 800 nm bands. The data sets are offset vertically for clarity. (d) Proposed upconversion path.

cay measurements are performed by uniformly exciting a fundamental WGM at 1473.4 nm with 10-ns square pulses and a peak absorbed power of 21.7 μW. Because of the weak PL signal, we apply a pulse-delay technique and a single photon counter to sample the C/L-band fluorescence decay curve [Fig. 4]. To reduce dark counts, InGaAs/InP avalanche photodiodes (APDs) are only gated above the breakdown voltage for a short time ($\sim$50 ns), which is not suitable for decay curves with 10^{-6}–10^{-2} s lifetimes. To circumvent the APD's narrow gate width, we use the 50-ns window to discretely sample the decay curve. Centering the arrival of a pump pulse in the detection window simultaneously acquires the PL's rise and initial decay due to the N^{th} pulse along with the decay associated with the $(N-1)^{th}$ pulse. The appearance of the N^{th} pulse serves as a marker for sampling the $(N-1)^{th}$ decay curve at a fixed delay—i.e. the pulse period separates the $(N-1)^{th}$ peak from its tail just before the N^{th} pulse. Several histograms (128 ps/bin resolution) with varying delays are used to construct the fluorescence decay in Fig. 4. As the pulse period approaches the PL lifetime, the data deviates from a single exponential curve because decay from multiple pulses contributes to the PL tail prior to the N^{th} pulse's arrival. Data at longer periods is limited by a constant noise floor linked to the small portion of pump laser spontaneous emission that is not blocked by the filters. For $\tau_{\text{eff}} \approx 10\,\mu$s, probabilistic simulation suggests that a fitting region of 10–20 μs gives the greatest confidence unbiased estimate of the decay lifetime. Fitting the points in this range gives an effective lifetime of $5.7\pm0.9\,\mu$s for a peak excitation of 21.7 μW and $\pm2\sigma$ uncertainty. With the effective lifetime much lower than the measured 8 ± 0.5 ms (7.8 ± 2.2 ms calculated) radiative lifetime in lightly Er^{3+}-doped bulk Y_2O_3 [39], nonradiative relaxation is a major concern.

The nonradiative decay of rare-earth ions was extensively investigated during the early development of inorganic gain crystals for solid-state lasers, and accurate phenomenological models have been established to describe the two principal mechanisms: multiphonon relaxation and cooperative relaxation (also known as concentration quenching) [40]. For multiphonon emission, the high yield of the $^4I_{13/2}\rightarrow{}^4I_{15/2}$ transition in low Er^{3+}-density samples is because the 0.8 eV (6500 cm^{-1}) energy gap is too large for fast depopulation. Using parameters from Er^{3+}

#100542 - $15.00 USD Received 25 Aug 2008; revised 6 Nov 2008; accepted 8 Nov 2008; published 12 Nov 2008

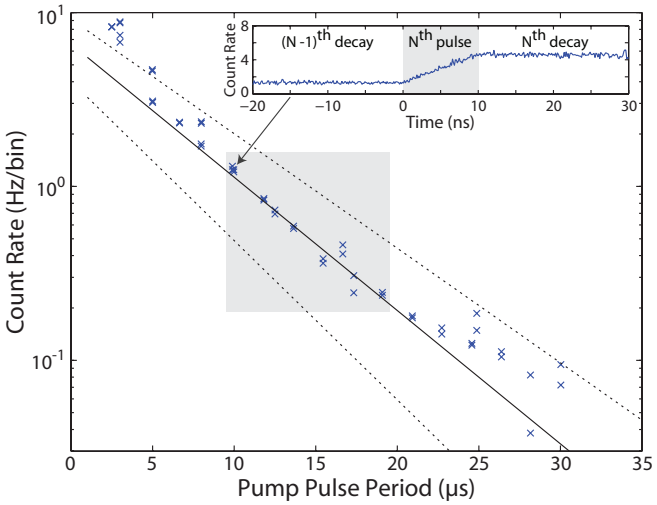

Fig. 4. Measurement of $^4I_{13/2}$ lifetime. Pulse period measurement of the lifetime for C/L-band emission. Fitting the data in the shaded area gives a lifetime of $5.7\pm0.9\,\mu$s; this uncertainty and the dashed curves mark $\pm2\sigma$ confidence for the fit. Inset: sample histogram for a pulse period of 9.89 μs (101.1 kHz repetition rate).

relaxation in Y_2O_3 at low temperature [39,41] and the close similarity of the Er_2O_3 and Y_2O_3 vibrational spectra [42], we estimate an effective lifetime of 4.2 s for relaxation at 300 K via emission of 12 phonons ($\sim$550 cm^{-1}). Cooperative relaxation encompasses several decay and sensitizing mechanisms where the excitation is nonradiatively transfered between ions through multipole or exchange interactions—we will limit the discussion to processes involving a single ion species. Self-quenching, where a donor ion decays to an intermediate level by exciting a low-level transition in another, is significant for higher levels in Er^{3+} (e.g. $^4S_{3/2}$) [43], but it is inactive for the first excited level ($^4I_{13/2}$). The most probable relaxation path in Er_2O_3 is the loss of energy to quenching (acceptor) sites either from direct transfer or from resonant excitation migration through multiple ions [44]. Acceptors are usually nonluminescent impurities (1–10 ppm of Fe, W, and Re and $>$10 ppm of Ta are present in the erbium source, impurity levels in the final Er_2O_3 films are unknown) and/or perturbed electronic states near surfaces or dislocations. At time scales shorter than the radiative lifetime in high purity crystals at 300 K, diffusion via electric dipole-dipole interactions becomes extremely rapid and $>10^5$ transfers are possible before reaching an acceptor [45,46]. Although transfer through $(Y_{1-x}Tb_x)_3Al_5O_{12}$ ($0.1 \leq x \leq 1.0$) was consistent with dipole-dipole coupling [47], high donor concentrations, as in Er_2O_3, may further the increase migration rate through short-range exchange and/or electric quadrupole-quadrupole interactions [48]. This transfer rate and the nonradiative relaxation can be slowed by increasing the mean Er–Er separation. Assuming the decay is diffusion-limited due to a low density of acceptors and conservatively assuming dipole-dipole interactions, the nonradiative decay rate is proportional to the Er^{3+} concentration [46,49].

3.4. Power-dependent radiative efficiency

The C/L-band radiative efficiency ($\eta_{\rm obs}$) for emission into the observed WGMs can be accurately determined by integrating the collected PL, correcting for collection losses, and dividing by the absorbed CW power (see §A.4). We analyze the power-dependence of $\eta_{\rm obs}$ for several

#100542 - $15.00 USD Received 25 Aug 2008; revised 6 Nov 2008; accepted 8 Nov 2008; published 12 Nov 2008

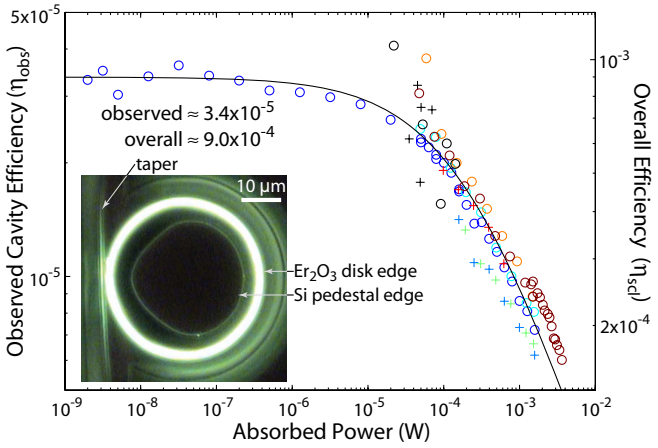

Fig. 5. Radiative efficiency of the ${}^4I_{13/2} \rightarrow {}^4I_{15/2}$ transition vs. absorbed pump power. The marker color indicates the pump-mode wavelength from blue (1460.9 nm) to dark red (1494.5 nm) while ($\circ$) and ($+$) designate first- and second-order radial pump modes, respectively. Black markers represent data from devices on another wafer processed with wet chemical etching and using first- and second-order pump modes (spanning 1437.6–1490.9 nm). The inset shows green upconverted luminescence from a fundamental cavity mode.

pump modes across the S-band on two different samples. In Fig. 5, $\eta_{\rm obs}$ decreases as upconversion becomes the dominant path for depopulating ${}^4I_{13/2}$; at $204\pm47\,\mu$W there are equal rates for nonradiative relaxation and cooperative upconversion. We use the pump power dependence of $\eta_{\rm obs}$ and the $5.7\pm0.9\,\mu$s fitted lifetime to give a zero-power effective ${}^4I_{13/2}$ lifetime of $\tau_{\rm o} = 7.2\pm1.2\,\mu$s. Since the radiative lifetime ($\tau_{\rm rad}$) in these Er_2O_3 films should be very similar to the 8 ms lifetime in Y_2O_3 [39], $\tau_{\rm o}$ can be related to the overall emission efficiency across the S/C/L-bands ($\eta_{\rm scl}$) and the observed spontaneous emission coupling-factor ($\beta_{\rm obs}$) for the chosen cavity resonances:

$$\tau_{\rm o}/\tau_{\rm rad} = \eta_{\rm scl} = \eta_{\rm obs}/\beta_{\rm obs}. \tag{1}$$

With $\tau_{\rm o} = 8$ ms and $\eta_{\rm obs} = 3.4\times10^{-5}$, we find $\eta_{\rm scl} = 9.0\times10^{-4}$ and $\beta_{\rm obs} = 0.038$, which is consistent with estimates of $\beta_{\rm obs}$ based on the cavity mode spectrum and negligible Purcell enhancement of $\tau_{\rm rad}$ (see §A.5). Finally, at $204\,\mu$W, upconversion reduces the lifetime to $\tau_{\rm eff} = \frac{1}{2}\tau_{\rm o}$ and gives $\sim3\times10^{20}$ ions/cm^3 in ${}^4I_{13/2}$. Based on the more rigorous analysis of Nikonorov et al. [50], we estimate the cooperative upconversion coefficient ($C_{\rm up}$) to be

$$C_{\rm up} = \frac{2hcV}{\lambda_{\rm p}\tau_{\rm o}^2 P_{\rm up}} = (5.1\pm2.1)\times10^{-16}\,{\rm cm}^3/{\rm s}, \tag{2}$$

where $V = 20.1\,\mu{\rm m}^3$ is the volume of Er_2O_3 excited by the cavity mode, $\lambda_{\rm p} \approx 1480$ nm is the pump wavelength, and $P_{\rm up} = 204\pm47\,\mu$W is the power when the nonradiative and upconversion rates are equal. This upconversion coefficient is extremely large and similar to that found in co-sputtered Er_2O_3/Al_2O_3 [51].

4. Conclusions

Due to upconversion and nonradiative relaxation, rate equation estimates suggest significant power is required to invert the ${}^4I_{15/2}$ manifold in these 20-μm microdisk cavities (see §A.6).

#100542 - $15.00 USD Received 25 Aug 2008; revised 6 Nov 2008; accepted 8 Nov 2008; published 12 Nov 2008

Since the large upconversion rate prevents transparency in the C-band until most of the electrons are sequestered in higher states, individual upper levels (e.g. $^2H_{11/2}$) may be the first to invert relative to the ground state, making Er_2O_3 upconversion green lasers a possibility [52–54]. EOS might also be developed into an incoherent visible emitter—rough estimates based on the camera's sensitivity give a green radiative efficiency on the order of 5% for an absorbed power density of 0.15 mW/μm^3. Additionally, we are investigating the potential of Er_2O_3 to upconvert infrared radiation into the visible spectrum for use in multijunction silicon solar cells.

To achieve technological maturity for its original application to waveguide amplifiers and lasers for on-chip optical networks, we are working to address the material's optical inefficiencies (upconversion and nonradiative relaxation) and to develop methods for electrical injection. We are exploring the growth of ternary alloys with Y and Gd to slow the upconversion and nonradiative processes by increasing the inter-ion separation—e.g. $(Y_{0.9}Er_{0.1})_2O_3$ may exhibit resonant absorption on the order of 36 dB/cm with significantly improved C/L-band radiative efficiency. Detailed studies (as in Ref. [49]) of high quality Er_2O_3 and $(Y_{1-x}Er_x)_2O_3$ films will be necessary to characterize the energy migration and quenching sites, but this information is necessary to optimize the Er^{3+} concentration for performance of on-chip amplifiers (gain, efficiency, etc.). We are also working to grow $(RE)_2O_3$-Si superlattices and to determine how the Er^{3+} $4f$-levels align relative to the Si bands. As in III-V systems, high quality epitaxy will become crucial in controlling the material's structure and optical properties while moving toward CMOS-compatible electroluminescence and photodetection.

A. Appendix

This document contains details for (A.1) x-ray diffraction analysis, (A.2) fiber-taper measurements of microdisk cavity transmission and photoluminescence while (de)muxing the pump and emission wavelengths, (A.3) fitting cavity loss rates and non-Lorentzian resonances, (A.4) determining the radiative efficiency for cavity-mode coupled emission using measured parameters, (A.5) estimating the ratio of free-space and cavity-coupled emission, and (A.6) our toy three-state rate equation model.

A.1. X-ray diffraction analysis

We employ two configurations for XRD analysis using a standard Cu K_α source: (1) a low angular resolution configuration that is sensitive to more material phases and (2) a high angular resolution configuration. The low-resolution setup utilizes a mirror to provide a wider angular divergence and higher intensity (shorter integration times) for the X-rays. With the $\langle 110 \rangle$ wafer flat of the Si(111) substrate 30° misaligned from the X-ray beam, this measurement is sensitive to more secondary material phases as in Fig. 1(b). The high resolution setup aligns the wafer flat parallel to the X-ray beam and uses a monochromator to narrow the beam's angular divergence. High-resolution XRD spectra only include the Si$\{111\}$ and $Er_2O_3\{111\}$ peaks.

A.2. Experimental setups for taper-based measurements

All the major optical measurements in this work are diagramed in Fig. 6. While these configurations are fairly self-evident, there are a few points that may need clarification.

- Two complementary VOAs are used to maintain a constant optical power at the photodetector (to give a constant electronic noise level) while the power at the device can be varied over 60 dB [55]. To avoid any nonlinear effects or absorption saturation while acquiring transmission spectra, the lasers are usually attenuated to give $\sim$200 nW at the taper, of which $\sim$10% is coupled into the microdisk cavity.
- We employ a fiber-based MZI for sub-picometer calibration of narrow cavity linewidths.

#100542 - $15.00 USD Received 25 Aug 2008; revised 6 Nov 2008; accepted 8 Nov 2008; published 12 Nov 2008

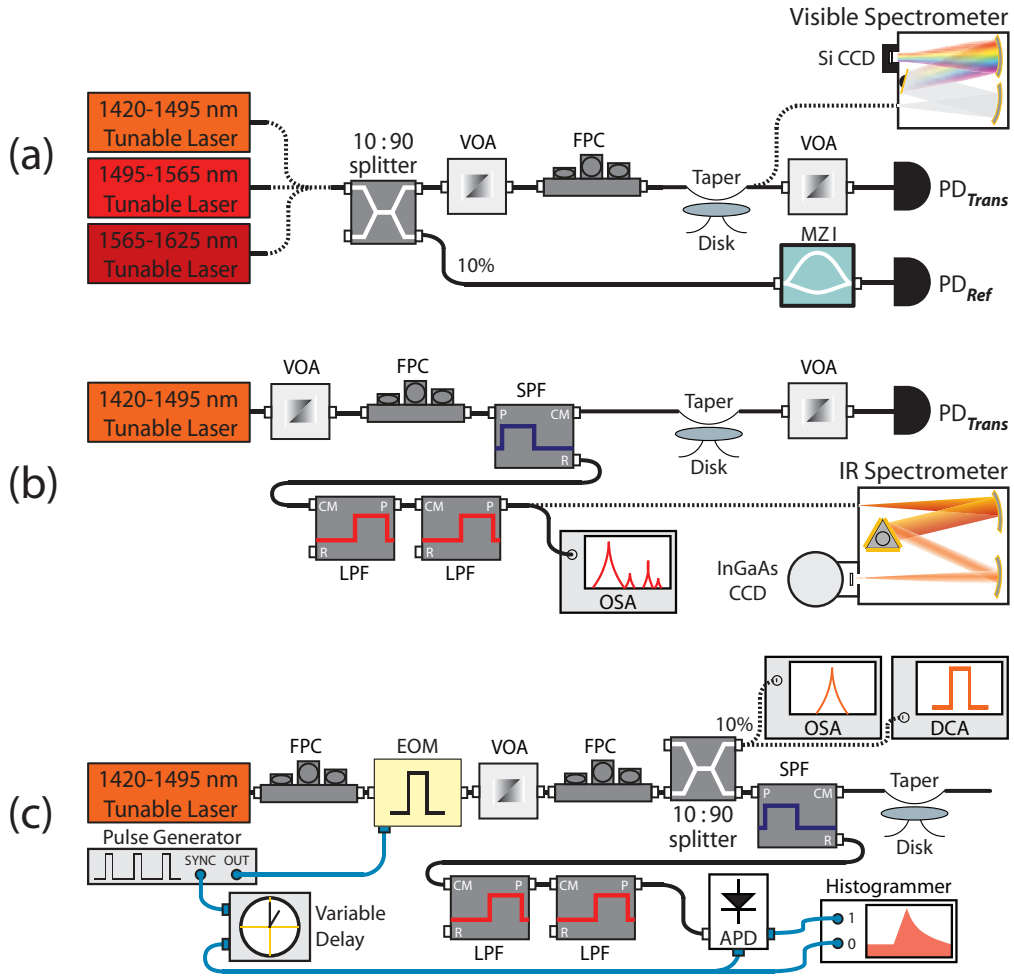

Fig. 6. Testing arrangements for measuring (a) cavity transmission spectra and visible upconversion, (b) C/L-band photoluminescence and radiative efficiency, and (c) ${}^4I_{13/2} \rightarrow {}^4I_{15/2}$ effective lifetime. Abbreviations: variable optical attenuator (VOA), fiber polarization controller (FPC), Mach-Zehnder interferometer (MZI), photodetector (PD), short-pass filter (SPF, pass 1460–1500 nm, reflect 1527–1610 nm), long-pass filter (LPF, pass 1527–1610 nm, reflect 1455–1500 nm), optical spectrum analyzer (OSA), digital communications analyzer (DCA), electro-optic modulator (EOM), and InGaAs/InP avalanche photodiode (APD). Black lines represent optical fiber; blue lines designate coaxial cable. Dashed lines correspond to alternative connections.

#100542 - $15.00 USD Received 25 Aug 2008; revised 6 Nov 2008; accepted 8 Nov 2008; published 12 Nov 2008

- A fourth laser (spanning 1480–1580 nm) is used to study any resonances at the boundaries of the primary lasers' sweep ranges (i.e. near 1495 nm and 1565 nm).

- Utilizing wide band-pass filters, S-band transmission and C/L-band emission can be observed simultaneously [Fig. 6(b)]—all cavity-based PL measurements are pumped on resonance with a WGM. The long-pass and short-pass filters separate their pass bands ($P \leftrightarrow CM$ ports) and reflection bands ($R \leftrightarrow CM$ ports) with high directivity ($>$55 dB) and low insertion loss ($<$1 dB). By collecting and filtering PL in the cavity's "reflection" channel, we achieve $>$100 dB isolation at the pump wavelength. Some residual spontaneous emission from the laser diode does bleed through the filters and produces a $\sim$10 pW signal at 1519 nm with our pump near maximum power.

- Previous work has demonstrated that the total collection efficiency for the taper waveguide and WGMs is on the order of 10% [35]. While in contact with unpatterned undercut films, the taper collects $\sim$0.1% [56]. We use an optical spectrum analyzer to measure the PL at peak powers $\gtrsim$10 pW and a spectrometer with a liquid-N_2 cooled InGaAs detector array at lower powers.

- For cryogenic experiments, the fiber-taper waveguide and the sample are mounted on piezo-electric stages within a continuous flow ^{4}He cryostat [57].

- During pulsed emission measurements in Fig. 6(c), two polarization controllers are needed to independently match the polarizations of the EOM and the cavity resonance. To optimize the modulator bias voltage and input polarization, we constantly monitor our extinction ratio ($>$35 dB) and pulse shape (square pulse, 100 ps rise time, 120 ps fall time) with an OSA and a DCA.

- A variable electronic delay is necessary to synchronize the APD with the arrival of the PL pulse and to avoid effects associated with ringing in the gate voltage as in Ref. [58].

A.3. Cavity mode spectra and lineshapes

The whispering gallery mode spectrum for microdisk optical resonators can be modeled semi-analytically using an effective index approximation [33, 59, 60] or numerically using finite-element simulations. A radius of $\sim$20 μm and thickness of 150 nm are chosen to give minimal bending loss across the S/C/L-bands and well separated first- and second-order radial modes, as in Fig. 7(a). Conveniently, these cavity modes and the taper waveguide are almost phase matched, which gives near critical coupling for a wide range (1450–1560 nm) when the taper is placed in contact with the disk edge. The shallower transmission features near 1535 nm and 1549 nm are attributed to single-pass absorption in the waveguide-cavity coupling region.

The cavity-waveguide coupling is commonly described using coupled mode theory [61]. Since the Er^{3+} absorption dominates coherent backscattering [62, 63], we restrict our analysis to a single traveling-wave whispering gallery mode. Adopting the phase convention of Ref. [64], the equation of motion for the clock-wise mode amplitude a_{cw} is

$$\frac{d}{dt}a_{\mathrm{cw}} = -i\Delta\omega a_{\mathrm{cw}} - \frac{1}{2}(\gamma_{\mathrm{i}} + \gamma_{\mathrm{e}})a_{\mathrm{cw}} + \kappa s \tag{3}$$

where $\Delta\omega = \omega - \omega_0$ is the detuning; $\gamma_{\mathrm{i}} = \gamma_{\mathrm{a}} + \gamma_{\mathrm{ss}} + \gamma_{\mathrm{rad}} + \ldots$ is the intrinsic power loss rate due to the sum of losses from absorption (γ_{a}), surface scattering (γ_{ss}), radiation (γ_{rad}), etc.; γ_{e} is the extrinsic coupling rate to the waveguide; and s is the amplitude of the waveguide field. The intrinsic and loaded cavity quality factor (Q_i and Q_l) are given by $\omega_0/\gamma_{\mathrm{i}}$ and $\omega_0/(\gamma_{\mathrm{i}} + \gamma_{\mathrm{e}})$, respectively. Under a weak coupling approximation, time reversal symmetry and conservation

#100542 - $15.00 USD Received 25 Aug 2008; revised 6 Nov 2008; accepted 8 Nov 2008; published 12 Nov 2008

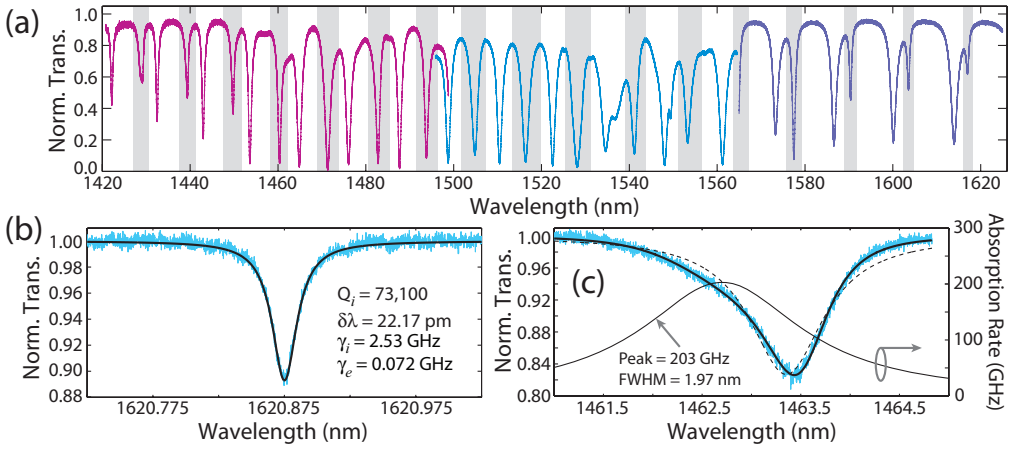

Fig. 7. (a) Microdisk transmission spectrum for quasi-TE modes; the fundamental radial-order WGMs are highlighted (grey). (b) Sample Lorentzian fit. (c) Sample non-Lorentzian fit (solid line) of an asymmetric cavity resonance. The inferred absorption peak and a Lorentzian fit (dashed line) to the same data are also included.

of power require the coupling coefficient (κ) to satisfy $\kappa = i\sqrt{\gamma_e}$. Ignoring any parasitic loading [65], the normalized cavity-waveguide transmission (T_{cav}) in steady state is

$$T_{cav} = \left|1 + i\sqrt{\gamma_e}\left(\frac{a_{cw}}{s}\right)\right|^2 = \left|1 - \frac{\gamma_e}{i\Delta\omega + \frac{1}{2}(\gamma_i + \gamma_e)}\right|^2. \quad (4)$$

To obtain the best estimate for γ_i, we weakly load the cavity ($\sim$10% contrast) and fit the data with Eq. (4) to find $\{\omega_0, \gamma_i, \gamma_e\}$, as in Fig. 7. For a fixed taper position, WGMs across the S/C/L bands exhibit different coupling depths because of the Er^{3+} absorption spectrum. On the edges of the absorption band (near 1420 nm and 1620 nm), $\gamma_i \ll \gamma_e$, and the resonances are significantly over coupled. In the center of the band, $\gamma_i \approx \gamma_e$, and the modes are near critical coupling.

Since there are several loss mechanisms that contribute to γ_i, radiation and surface scattering losses must be accounted for when using cavity modes to determine the absorption spectrum (similar to [66]). By choosing appropriate cavity dimensions, the calculated γ_{rad} is negligible for the fundamental modes: $\gamma_{rad} < 82\,\text{MHz} = 0.026\,\text{cm}^{-1}$. Since Rayleigh scattering increases towards longer wavelengths [59,67], scattering losses can be bounded as less than the minimum intrinsic loss rate near 1625 nm: $\gamma_{ss} \lesssim \min(\gamma_i) = 2.5\,\text{GHz} = 0.79\,\text{cm}^{-1}$. This 2.5 GHz likely has a small absorption component as ${}^4I_{13/2} \rightarrow {}^4I_{15/2}$ emission into WGMs is observed out to $\sim$1660 nm. Therefore scattering accounts for less than 1% of the peaks, and $\gamma_i \approx \gamma_a$ except in the spectral tails. The second-order microdisk resonances exhibit slightly greater γ_i's due to mode coupling between the Er_2O_3 WGMs and the lossy WGMs of the Si pedestal. Because we are unable to bound this additional loss rate, the second-order modes are not used to establish the ${}^4I_{15/2} \rightarrow {}^4I_{13/2}$ absorption spectrum.

Due to the small inhomogeneous broadening of the Er^{3+} transitions, it is possible for an underlying absorption peak to change appreciably across a cavity linewidth. In this case, the resulting non-Lorentzian cavity resonance can be fit [Fig. 7(c)] using Eq. (4) and including a

#100542 - $15.00 USD Received 25 Aug 2008; revised 6 Nov 2008; accepted 8 Nov 2008; published 12 Nov 2008

Lorentzian absorption profile

$$\gamma_{\mathrm{i}} \approx \gamma_{\mathrm{a}}(\omega) = \frac{\gamma_0(\delta\omega_{\mathrm{a}}/2)^2}{(\omega-\omega_{\mathrm{a}})^2+(\delta\omega_{\mathrm{a}}/2)^2} \tag{5}$$

where ω_{a}, $\delta\omega_{\mathrm{a}}$, and γ_0 are the center, full width at half-maximum, and amplitude of the absorption peak. For the observed resonances, it has been unnecessary to include the absorption peak's effect on the real part of the refractive index through the Kramers-Kronig relation. The inferred absorption peaks from fitting these asymmetric resonances around 1457.3, 1462.8, 1478.8, 1545.6, and 1556.9 nm agree well with the data from nearby Lorentzian resonances.

A.4. Radiative efficiency measurement

Because the fiber taper offers adjustable waveguide coupling and a low-loss method for PL excitation and collection [35], the efficiency for emission into the cavity modes can be empirically determined. The cavity-coupled radiative efficiency (η_{obs}) is given by the ratio of the *total* power emitted into the cavity modes divided by the *absorbed* pump power. This measurement requires careful characterization of the pump mode along with all modes in the desired emission band. For these c-Er_2O_3 microdisks, surface scattering and radiation losses are negligible compared to the Er^{3+} absorption, and the absorbed power (P_{a}) is nearly equal to the dropped power (P_{d})

$$P_{\mathrm{a}} = \frac{\gamma_{\mathrm{a}}}{\gamma_{\mathrm{i}}}P_{\mathrm{d}} \approx P_{\mathrm{d}} = (1-T_{\mathrm{cav}})\frac{P_{\mathrm{in}}}{\sqrt{T_{\mathrm{t}}}} \tag{6}$$

where T_{cav} is the cavity-waveguide transmission at the pump wavelength, T_{t} is the end-to-end fiber taper transmission, and P_{in} is the pump power measured at the fiber taper input. Equation (6) assumes the taper's loss is symmetric about the taper-device coupling region. While transmission loss in fiber tapers is usually dominated by bending loss in the taper mount which is symmetric about the coupling region, small bits of dust on the taper will scatter light from the fundamental mode and produce asymmetric loss. In this case, $\sqrt{T_{\mathrm{t}}}$ is replaced by the one-sided waveguide transmission (T_1), which can be found from T_{t} and the ratio of another quantity that depends on P_{d} (e.g. thermo-optic wavelength shift, peak PL yield, etc.) when using either end of the waveguide as the input. For these measurements, $T_{\mathrm{t}} = 0.68$ with symmetric losses. Using the collected emission [$P(\lambda)$] spectrum as in Fig. 8, the total power emitted into the cavity modes (P_{cav}) is given by

$$P_{\mathrm{cav}} = \frac{2}{\delta\lambda_{\mathrm{rbw}}\sqrt{T_{\mathrm{t}}}}\Big[\sum_n\big(\frac{\gamma_{\mathrm{i},n}+\gamma_{\mathrm{e},n}}{\gamma_{\mathrm{e},n}}\big)\int\frac{P_n(\lambda)}{T_{\mathrm{f}}(\lambda)}d\lambda\Big] \tag{7}$$

where the summation is over the cavity modes at $\lambda > 1520$ nm and $\delta\lambda_{\mathrm{rbw}}$ is the resolution bandwidth of the detector. The factor of 2 compensates for equal emission into the degenerate clockwise and counter-clockwise traveling-wave modes of the disk and hence into the forward and backward propagating modes of the waveguide. While the C/L-band transmission [$T_{\mathrm{f}}(\lambda)$] is fairly flat for the filters used to (de)mux the PL and the pump beam, the transmission does slowly decrease at longer wavelengths. In the emission band, $T_{\mathrm{t}} = 0.66$ with symmetric loss. To establish and correct for the fraction of the PL in the WGMs that is collected by the taper, we find the total cavity loss rate for *each* cavity mode in the emission band by measuring the $\gamma_{\mathrm{i},n}$ under weak loading and $\gamma_{\mathrm{e},n}$ at the fixed taper position used during PL collection. Then the fraction of P_{cav} coupled into the forward propagating mode is the ratio of the loss rate into the waveguide ($\gamma_{\mathrm{e},n}$) over the loss rate into all channels ($\gamma_{\mathrm{i},n}+\gamma_{\mathrm{e},n}$), which gives a correction factor of $(\gamma_{\mathrm{i},n}+\gamma_{\mathrm{e},n})/\gamma_{\mathrm{e},n}$. Since the ratio of the intensity of individual WGMs over the total emitted power is constant at $P_{\mathrm{d}} \lesssim 4$ mW, the total integrated PL is proportional to the intensity of the

#100542 - $15.00 USD Received 25 Aug 2008; revised 6 Nov 2008; accepted 8 Nov 2008; published 12 Nov 2008

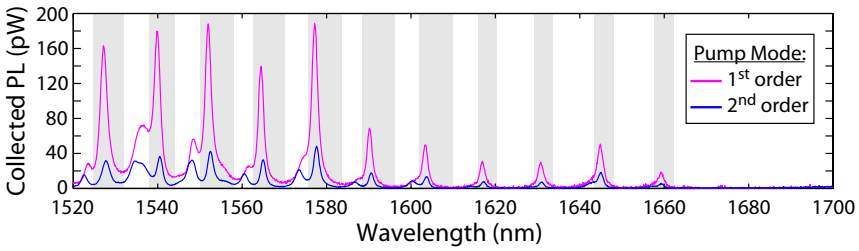

Fig. 8. Observed cavity-coupled photoluminescence spectrum for the device in Fig. 7(a); the fundamental WGMs are highlighted (grey).

strongest emission line. Using this proportionality, the radiative efficiency measurement can be extended to excitation levels low enough that the largest PL peak is just above the noise floor.

A.5. β-factor calculation

In laser physics, the β-factor is the ratio near the lasing threshold of the spontaneous emission into the lasing mode to the emission into all modes, and it can range from 10^{-6}–10^{-5} for large gas lasers to nearly 10^{0} for few quantum-dot microcavity lasers [68]. In this work, we modify this definition so β is the ratio of emitted power into a chosen subset of modes ($P'_{c,T}$) over the total power emitted into free-space ($P_{fs,T}$) and cavity modes ($P_{c,T}$):

$$\beta = \frac{P'_{c,T}}{P_{fs,T} + P_{c,T}}. \tag{8}$$

From Fermi's Golden rule, the total emitted power (P_T) in a given spectral range is approximately

$$P_T = \frac{2\pi}{\hbar} \int \rho_f \left| \langle \psi_f | \hat{H}_{int} | \psi_i \rangle \right|^2 N_{\mathrm{Er}} \hbar \omega_i d\omega_i \tag{9}$$

where ρ_f is the density of final states and N_{Er} is the number of excited Er^{3+} ions. We express the final density of states as a product of the density of electronic states (ρ_e) per energy per ion and the density of emission modes (ρ_m) per unit frequency. Using a semiclassical electric-dipole interaction $\hat{H}_{int} = -q\vec{E} \cdot \vec{r}$ and averaging over all polarizations and wave vectors for a fixed dipole orientation, P_T can be expressed as

$$P_T = \frac{2\pi}{3\hbar} \int \rho_f \left| \langle \vec{E}(\omega_i) \rangle \right|^2 \left| \vec{\mu}(\omega_i) \right|^2 N_{\mathrm{Er}} \hbar \omega_i d\omega_i \tag{10}$$

where $\langle \vec{E}(\omega_i) \rangle$ is the time-averaged electric-field strength per emitted photon and $\vec{\mu}(\omega_i) = -q\langle \psi_f | \vec{x} | \psi_i \rangle$ is the $|\psi_i\rangle \rightarrow |\psi_f\rangle$ transition's dipole moment. For emission into free-space modes, ρ_m and $\langle \vec{E}(\omega_i) \rangle$ are given by

$$\rho_m = \rho_{fs}(\omega_i) = \frac{V_b \omega_i^2 n^3}{\pi^2 c^3} \tag{11}$$

$$|\langle \vec{E}(\omega_i) \rangle| = \sqrt{\frac{\hbar \omega_i}{2n^2 \varepsilon_o V_b}} \tag{12}$$

where V_b is the volume of the "box" containing the free-space modes and $n \approx 2.0$ is the refractive index of Er_2O_3. Since Eq. (10) for the free-space modes is proportional to the

#100542 - $15.00 USD Received 25 Aug 2008; revised 6 Nov 2008; accepted 8 Nov 2008; published 12 Nov 2008

measured photoluminescence spectrum from the unpatterned film, the spectral dependence of $\rho_e(\omega_i)|\vec{\mu}(\omega_i)|^2$ is known without obtaining its explicit form.

For emission into the microdisk cavity modes, ρ_m is

$$\rho_m = \rho_c(\omega_i) = \sum_j 2\mathbb{L}(\omega_i, \omega_j, \delta\omega_j) \tag{13}$$

where $\mathbb{L}(\omega_i, \omega_j, \delta\omega_j)$ is a lorentzian with a center at the j^{th} cavity mode (ω_j) and full-width at half-max ($\delta\omega_j$) given by the mode's loaded linewidth ($\gamma_e + \gamma_i$); $\mathbb{L}(\omega_i, \omega_j, \delta\omega_j)$ is normalized such that $\int_{-\infty}^{+\infty} \mathbb{L}(\omega_i) d\omega_i = 1$. The factor of 2 accounts for the degenerate clockwise and counter-clockwise traveling wave modes. Since the cavity field is not spatially uniform, the average field strength per photon in the j^{th} cavity mode experienced by the ions is

$$|\langle \vec{E}(\omega_i) \rangle_j| = \sqrt{\frac{\hbar\omega_i \vartheta_j}{2n^2 \varepsilon_o V_{c,j}}} \tag{14}$$

where $V_{c,j}$ is the cavity mode volume and ϑ_j accounts for the overlap between the j^{th} emission mode and the distribution of excited ions. Because the excited ion distribution depends on the intensity of the pump mode and Eq. (10) includes $|\langle \vec{E}(\omega_i) \rangle_j|^2$, ϑ_j is a scalar integral over the cavity volume

$$\vartheta_j = \frac{\int |\vec{E}_j|^2 |\vec{E}_p|^2 dV}{\max(|\vec{E}_j|^2) \int |\vec{E}_p|^2 dV} \tag{15}$$

with the field components of the pump mode ($\vec{E}_p$) and j^{th} emission mode ($\vec{E}_j$) computed with finite-element models.

Using the thin film PL data and the cavity mode parameters, the β-factor can be calculated for any individual or collection of modes. While $P_{c,T}$ in Eq. (8) includes a summation over all cavity modes (both observed and unobserved [69]), the $\vartheta_j / V_{c,j}$ factor heavily weights the contribution of the modes with low radial order. In this analysis we include the quasi-TE modes of the first 8 radial families; the quasi-TM modes are poorly confined and have little overlap with the Er^{3+} ions. For first and second radial-order emission modes at $\lambda > 1520$ nm as in the radiative efficiency measurement, we estimate $\beta_{\text{obs}} = 0.091$ which is in reasonable agreement with the experimental value of 0.038. Increasing the sum to include all observed modes across the S/C/L-bands (Fig. 7) gives $\beta_{12} = 0.127$. By including all the cavity modes in $P'_{c,T}$, $\beta_{\text{T}} = 0.227$ is the fraction of the total ${}^4I_{13/2} \rightarrow {}^4I_{15/2}$ photoluminescence that is emitted into the microdisk WGMs.

A.6. Three-state rate equation model

To model the upconversion and nonradiative relaxations of the ${}^4I_{13/2}$ population, we solve a three-state system of rate equations in the steady state:

$$N_1 = N_{\text{Er}} - N_2 - N_3 \tag{16}$$

$$\frac{dN_2}{dt} = -\frac{N_2}{\tau_o} - C_{\text{up}} N_2^2 + s\Phi(N_1 - rN_2) \tag{17}$$

$$\frac{dN_3}{dt} = -\frac{N_3}{\tau_o} + \frac{1}{2} C_{\text{up}} N_2^2. \tag{18}$$

The populations $\{N_1, N_2, N_3\}$ represent densities for ions in the $\{{}^4I_{15/2}, {}^4I_{13/2}, {}^4I_{9/2}\}$ states, respectively; higher states are neglected because we lack reasonable estimates for the appropriate upconversion and/or excited-state absorption coefficients. For simplicity, the Stark-split structure for all levels is ignored. The total ion density on C_2 lattice sites (N_{Er}) is

#100542 - $15.00 USD Received 25 Aug 2008; revised 6 Nov 2008; accepted 8 Nov 2008; published 12 Nov 2008

$2.0\times10^{22}\,\mathrm{cm}^{-3}$, and we use our estimated value for the cooperative upconversion coefficient $C_{\mathrm{up}} = 5.1\times10^{-16}\,\mathrm{cm}^{-3}/\mathrm{s}$. We assume the ${}^4I_{13/2}$ and ${}^4I_{9/2}$ lifetimes are approximately equal ($\tau_{\mathrm{o}} = 7.2\,\mu\mathrm{s}$) because both transitions to the ground state are dipole forbidden and likely subject to similar nonradiative relaxation—spontaneous and stimulated emission are both excluded from this analysis. The pump photon flux within the cavity is given by Φ, and r is the ratio of the emission and absorption cross sections at the pump wavelength. For Er^{3+}-doped silica, $r \approx 1/3$ at 1480 nm [70]. The adjustable parameter $s = 2.5\times10^{-12}$ encompasses a number of factors including the value of the absorption cross section; it is set to give $N_2 \approx 2.0\times10^{20}\,\mathrm{cm}^{-3}$ at $P_{\mathrm{d}} = 204\,\mu\mathrm{W}$—corresponding to the inferred values from our radiative efficiency measurements. This model for the Er^{3+} transitions is then applied to a microdisk cavity (20-μm radius, 20.1-$\mu\mathrm{m}^3$ active volume).

Solutions to these rate equations give only a rough estimate for the pump powers at which $N_2 \approx N_3$ and at which these transitions near transparency. By $P_{\mathrm{d}} \approx 0.6\,\mathrm{mW}$, there are $\sim5\times10^{20}\,\mathrm{ions/cm}^3$ in both the ${}^4I_{13/2}$ and ${}^4I_{9/2}$ levels. These microdisks approach transparency for ${}^4I_{9/2}\rightarrow{}^4I_{15/2}$ ($\lambda \approx 800\,\mathrm{nm}$) and ${}^4I_{13/2}\rightarrow{}^4I_{15/2}$ ($\lambda \approx 1480\,\mathrm{nm}$) with pump powers of $P_{\mathrm{d}} \approx 18\,\mathrm{mW}$ and $P_{\mathrm{d}} \approx 130\,\mathrm{mW}$, respectively. To more accurately represent the system, this model should, at least, include higher energy levels. Since the upconverted luminescence is most intense around $\lambda \approx 550\,\mathrm{nm}$, the combined upconversion-emission path for ${}^4I_{9/2}\rightarrow{}^2H_{11/2}/{}^4S_{3/2}\rightarrow{}^4I_{15/2}$ may provide a fast route back to the ground state. A fast green relaxation would increase the transparency thresholds and may make the ${}^4I_{9/2}\rightarrow{}^4I_{15/2}$ relaxation a secondary process. In summary, the upconversion processes close to transparency may be quick enough to produce substantial populations in every level up to and including ${}^2H_{11/2}$, which greatly increases the number of spontaneous and stimulated relaxations that must be considered.

Acknowledgments

This work was funded by the DARPA EPIC program. We would like to thank Q. Lin for his fabrication assistance, and CPM would like to thank the Moore Foundation and the NSF for fellowship support.

#100542 - $15.00 USD Received 25 Aug 2008; revised 6 Nov 2008; accepted 8 Nov 2008; published 12 Nov 2008